

Dynamic Modelling and Control of Exoskeleton Gantry Robot

Eesha Hajare

Submitted under the supervision of Suhasa Kodandaramaiah to the University Honors Program at the University of Minnesota-Twin Cities in partial fulfillment of the requirements for the degree of Bachelor of Science, *summa cum laude*, in Mechanical Engineering.

8th May 2024

ACKNOWLEDGEMENTS

I would like to thank Professor Suhasa Kodandaramaiah and my graduate mentor, Pin-Hao Cheng for their exemplary mentorship and guidance throughout the process of completing this thesis, in addition to other researchers in the Biosensing and Biorobotics Laboratory for their support and camaraderie. I feel grateful to have been a part of such an innovative and kind group of individuals during my undergraduate research experience. I would also like to thank my thesis committee members, Professors Zongxuan Sun and Perry Li, for offering their expertise in the review of my work. Lastly, I would like to thank my family for supporting me throughout my undergraduate journey.

ABSTRACT

This thesis presents the development and analysis of a dynamic model for an exoskeleton gantry used to perform neuroscience experiments in freely moving mice. The dynamic model of the exoskeleton gantry, comprised of X and Y stages, is developed, and relevant system characteristics like bandwidth and stability are studied using a theoretical and experimental approach. The predicted bandwidth of the open-loop system, using the theoretical model, is found to be 1.9 Hz and 3.8 Hz for Stage X and Y, respectively. The open-loop system was further verified experimentally using LABVIEW, and system identification was performed using MATLAB. According to the experimental results, the open-loop bandwidth of the X and Y stages was found to be 2.3 Hz and 2.76 Hz, respectively. Furthermore, the gain and phase margin of the open-loop system is used to gauge the stability of the closed-loop system. According to the theoretical model, it is expected that the bandwidth of the open and closed-loop systems increases with a decrease in payload. The gain margin and phase margin, predicted theoretically and verified experimentally, are well above the determined threshold of 2 dB for gain margin and 45° for phase margin. This ensures the stability of the closed-loop exoskeleton system. Moreover, the closed-loop bandwidth of the system is predicted using the theoretical model, and an admittance control framework is proposed. The predicted closed-loop bandwidth for the exoskeleton gantry is found to be 19.2 Hz and 16.4 Hz for X and Y stages, respectively. Furthermore, preliminary experimentation of the gantry with admittance control implementation suggests a closed-loop bandwidth of 46Hz for Stage X.

TABLE OF CONTENTS

Chapter 1: Introduction	4
1.1 Overview	4
1.2 Background	6
Chapter 2: Dynamic Modelling Theory	8
2.1 Dynamic Modelling Overview	8
2.2 Permanent Magnet Linear Synchronous Motor Modelling	10
Chapter 3: Exoskeleton Gantry Modelling	14
3.1 Theoretical Model of Gantry	14
3.2 Admittance Control	20
Chapter 4: Experimental Verification	22
4.1 Experimental Set-Up and Data Processing	22
4.2 Results	24
4.3 Discussion	29
Chapter 5: Conclusion and Future Work	32
APPENDIX	
APPENDIX A – Theoretical Plant Transfer Function Derivation	
APPENDIX B – Experimental Results Processing Code	

Chapter 1: Introduction

1.1 *Overview*

Neuroscience aims to study the interactions between different brain regions when animals engage in complex behaviors. The neural connections of the brain are studied while animals interact with their environments and participate in natural behaviors like navigation and foraging. One such technique currently implemented to study mouse brains is in-vivo 2-photon calcium imaging^{1,2}, which involves using fluorescent molecules to detect a rise in calcium activity post-neuron firing. Developments in these areas have allowed neuroscientists to study multiple cells under a wide field of view and capture neural activity at a higher resolution. However, even though these imaging techniques have been effective in studying neural activity with sufficient resolution, they require mice to have their head fixed in place. This is because high-resolution microscopes are often bulky, and their use requires them to be fixed in place. This can be a challenge as complex activities like navigation, decision-making, and foraging require mice to be freely moving. Moreover, head fixation is not a natural state for mice, and scientists are interested in studying the brain activity of freely locomoting mice. To counter this challenge, various studies have used Virtual Reality (VR) techniques to conduct brain studies in freely moving mice.³ However, such techniques still lack vestibular inputs and restrict navigation behavior in mice.

Current research that has overcome this problem of head fixation in mice has utilized a miniaturized microscope mounted on the mouse skull to study brain activity in freely behaving mice. These devices, like the mini-mscope⁴, must be less than 10% of the mouse weight; this results in a significant reduction in the imaging resolution and a smaller field of view. Hence, there is a significant trade-off between high-resolution imaging and studying brain states in freely behaving mice engaging in complex activities.

Previously, a cranial exoskeleton using delta robot architecture has been devised as a mobile robot platform to study brain states in freely moving mice.⁵ The head stage on this device is modular and we can implement different neural recording modalities, for example: optical imaging head stage enables it to capture calcium activities from multiple neurons from different regions of the cortex, while the electrophysiology head stage enables it to insert neural probes in various regions of the cortex to gather electrophysiological data. In our project, a similar robot with a simpler robot architecture and a 2-photon microscope was developed to enable high-resolution cellular-level imaging in freely moving mice. A heavy load-bearing H-gantry with 3 degrees of freedom is used as an exoskeleton for the mouse while it explores an 8-shaped maze. However, due to the unique nature of this exoskeleton gantry, it is necessary to model this system to obtain insights that can help determine the gantry's response to external inputs.

This thesis aims to investigate the theoretical dynamic model of this exoskeleton system and assess the similarity between the real and theoretical models through system identification techniques. The theoretical dynamic model is studied to understand the system characteristics like stability in the usable frequency range, bandwidth, and system type. Experimental verification of the dynamic model is carried out by studying experimental motion data as system output after an excitation signal is provided as input. The experimental data is post-processed, and computer software is used to fit a transfer function. System characteristics obtained from the experimental data are studied and compared to those of the theoretical model. Furthermore, an admittance control framework is chosen for the exoskeleton, and experimental data with desired velocity as input and actual velocity data as output is gathered from the exoskeleton gantry. This is used to study the admittance control response of the exoskeleton in its anticipated operational environment.

1.2 Background

An exoskeleton was previously developed for neuroscience investigations in freely locomoting mice. This exoskeleton can sustain heavy payloads of optic systems used for cellular-resolution imaging. It consists of a mobile robot platform in the form of an H-gantry that is capable of 3 degrees of freedom - X, Y, and Yaw motion. The X and Y stages are driven by permanent magnet linear synchronous motors (800mm travel range, PI-USA, model: V-857.576023E0), while the yaw stage is driven by a rotational actuator (IntelLiDrives Rotary table, model: PSR-300) with infinite yaw rotation. The head stage, consisting of the imaging system, is mounted on the rotational stage. A rendering of the exoskeleton gantry is shown in Figure 1.21.

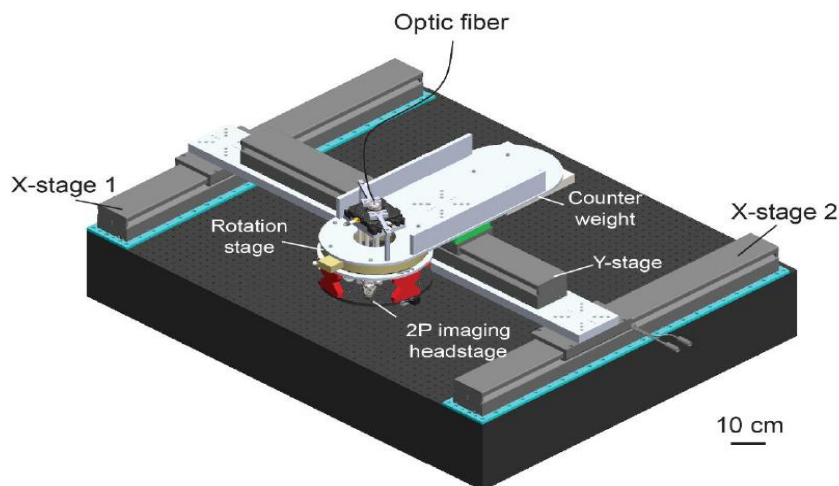


Figure 1.21 *High-level rendering of exoskeleton gantry.*

The exoskeleton is capable of supporting a payload of up to 27 kg from the head stage. The head stage consists of the 2P imaging system used to capture cellular and synaptic signals from the mouse brain when it navigates the arena. Since the center of mass of the payload is not aligned with Stage X, a counterweight is also added to the system to prevent stability issues from occurring. The mouse is connected to the gantry head stage with a titanium head post using a kinematic clamping mechanism, which allows it to transmit force. The mouse applies force through the

clamping mechanism to the exoskeleton to regulate its velocity and acceleration. A force sensor (ATI model: Nano17) with 6 degrees of freedom and a resolution of 6.25mN is attached to the clamping mechanism to measure the forces exerted by the mouse on the exoskeleton. These force measurements are used by a feedback controller to regulate the motion of the exoskeleton. The goal of the force-sensing feedback loop is to reduce the resistance and inertial forces experienced by the mouse. Reduction of the resistance force originating from the head stage will allow the mouse to achieve locomotion close to its natural locomotion in a free arena.

An admittance control strategy is used to reduce the resistance force experienced by the mouse. It uses the force exerted by the animal to determine the desired velocity or final position of the exoskeleton. An admittance controller is tuned beforehand to obtain the values of parameters necessary to obtain mouse locomotion trajectories using the exoskeleton gantry, similar to those in their freely behaving state. This tuning was carried out previously by mapping the trajectories of mice exploring the arena with the exoskeleton while the admittance control parameters were varied over multiple trials. Moreover, a Copley controller is used to control the velocity and acceleration of the exoskeleton in the absence of a mouse. This allowed the user to specify a desired velocity or position and study the response of the exoskeleton to the input. The Copley controller uses a Proportional and Integral (PI) controller for this purpose. The system identification of the exoskeleton uses LABVIEW to obtain the velocity/position response when an excitation signal is provided to the exoskeleton.

Chapter 2: Dynamic Modelling Theory

2.1 *Dynamic Modelling Overview*

A theoretical state-space model of the exoskeleton H-gantry is developed initially to study the expected system characteristics as well as provide inferences to the experimental system identification. Previous studies have considered multiple assumptions to simplify the problem. According to a study by Chen. R.et.al⁶, a dynamic model of an H-gantry was developed to characterize the vibrational patterns of flexible beams. Their model considers the presence of a lateral deflection in the Stage Y or the mid-axis of the gantry, which contributes to the creation of vibrations in the Stage Y along with the gantry motion at high frequencies. The motion equations for the final model are derived using the Lagrangian function. The developed model is a function of the gantry mass, stiffness of each axis, and the inertia of the gantry, where the mass, stiffness, and inertia are expressed as a function of admissible functions or the vibrational mode shapes of the gantry. Even though the complexity of this model allows the determination of the natural frequency mode shapes of the gantry, it does not consider the effect of heavy load on gantry motion, nor does it provide a suitable decoupling mechanism for our application.

Another study conducted by Qin. C et.al develops a model of an H-gantry driven by permanent magnet linear synchronous motors to propose a control system design.⁷ The model assumes mechanical coupling between the gantry axes, and equations of motion are derived with the

consideration of a deviation angle between the Stage X and the Stage Y. The equations of motion derived in this model are shown as corresponding to Figure 2.11. In this figure, the Y-axis

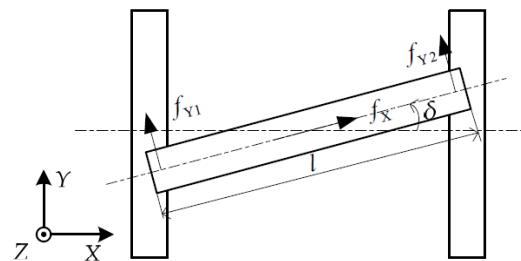


Figure 2.11 Free-Body Diagram of a simple H-Gantry (Qin et al., 2017)

corresponds to the parallel axes of the gantry, and the mid-axis corresponds to the X-axis. The moment caused by the thrust forces f_{y1} and f_{y2} acting on the Stage X causes it to tilt slightly by an angle delta (δ). The forces acting on the Stage X or the mid-axis are in the tilted coordinate system of the mid-axis. Force equations of motion obtained from the Qin. C gantry model are shown in the following equations.

$$m \ddot{y} = f_{y1} \sin\delta + f_{y2} \sin\delta + f_x \cos\delta \quad (2.11)$$

$$m \ddot{x} = f_{y1} \cos\delta + f_{y2} \cos\delta + f_x \sin\delta \quad (2.12)$$

$$J \ddot{\delta} = (f_{y2} - f_{y1}) \frac{l}{2} \quad (2.13)$$

In the above equations, m denotes the mass of the linear guides, J denotes the inertia, and l denotes the length of the Stage X linear guide. However, similar to the model by Chen. R et al, this model does not consider the effect of heavy load on the gantry. To consider the effect of heavy load on the gantry motion, Xie. H and Wang. Q modelled the gantry using a moving center of mass of the heavy load on the X-axis.⁸ The free-body diagram for Xie. H and Wang. Q model is shown in Figure 2.12.

In Figure 2.12, the Y-axis corresponds to the parallel axis of the gantry,

and the X-axis corresponds to the mid-axis. A load of mass(M) is situated on Stage X and is movable along the X-axis. The slight tilt in the Stage X due to the thrust forces is denoted by the angle (α). The thrust forces f_1 and f_2 act in the fixed coordinate system. The damping coefficients

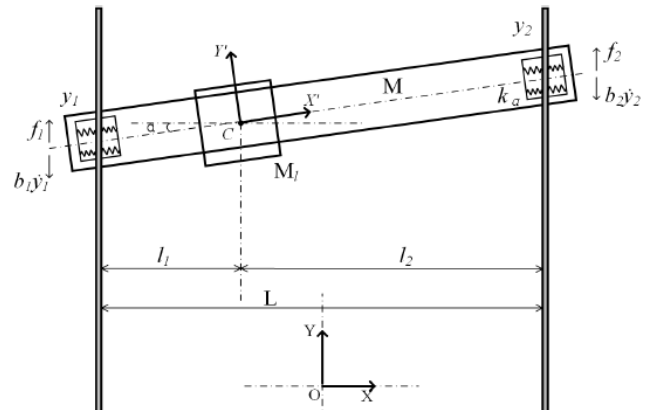


Figure 2.12 Free-body diagram of heavy load gantry. (Xie & Wang, 2022)

of the parallel Stage Y are shown as b_1 and b_2 , and the joints between the Stage Y and Stage X are modelled using a spring with stiffness K_a .

The center of mass of the load is calculated as: $y_c = \frac{l_1}{L}y_1 + \frac{l_2}{L}y_2$, and the tilt angle of the Stage X linear guide is calculated to be $\alpha = \frac{y_2 - y_1}{L}$. The equations of motion were derived for linear and rotational acceleration of the center of mass. The equations of motion for a heavy load gantry as given by Xie. H is shown below:

$$M\ddot{y}_c = f_1 + f_2 - (b_1 + b_2)\dot{y}_c + (b_1l_1 + b_2l_2)\dot{\alpha} \quad (2.14)$$

$$J\ddot{\alpha} = -f_1l_1 + f_2l_2 - (b_1l_1^2 + b_2l_2^2)\dot{\alpha} + (b_1l_1 + b_2l_2)\dot{y}_c - K_a\alpha \quad (2.15)$$

Where, J is the inertia of the guide rails and l_1, l_2 are the lengths of the ends of the guide rail from the load. This model accounts for heavy load on the gantry guide rails as well as provides a coupled model for guide rail actuation and suits our application for the exoskeleton system.

2.2 Permanent Magnet Linear Synchronous Motor Modelling (PMLSM)

The linear guide rails of the exoskeleton gantry are driven by permanent magnet linear synchronous motors. The output of the exoskeleton system is the velocity or position, and the input to the system is the commanded current to the motors. This input-output setup requires us to model a relation between the current command of the motor and its output velocity for permanent magnet linear synchronous motors.

Permanent magnet linear synchronous motors work on the principle of electromagnetism and convert electrical energy into linear mechanical motion. The moving rotor is comprised of permanent magnets, establishing a magnetic field, while the stationary stator is formed by coil windings. The stator windings are connected to a three-phase alternating current supply, which

generates a changing magnetic field. The magnetic field generated by the permanent magnet interacts with the magnetic field produced by the stator coils and induces an electromotive force that produces a linear motion. Hence, the electromotive force of the linear synchronous motors needs to be derived as a function of input current.

There are multiple approaches to model the permanent magnet linear synchronous motor's thrust force as a function of current. One such approach suggested by Miller C.E et.al includes assuming a permanent magnet linear synchronous motor to be a rotary motor that has been cut-down its radial surface and unrolled.⁹ This model derives the thrust force of PMLSMs in a two-axis reference frame or the travelling reference frame. A visual representation of the travelling reference frame and the stationary reference frame is shown in Figure 2.21.

As shown in Figure 2.21, in the travelling reference frame (dq-axis), the d-axis is aligned with the rotor's magnetic flux, and the q-axis is directly perpendicular to it. In the stationary reference frame (a-b-c axis), each axis is aligned with its respective current phase in the three-phase current system. The transformations between the stationary reference frame and the travelling reference frame are given by the Clarke

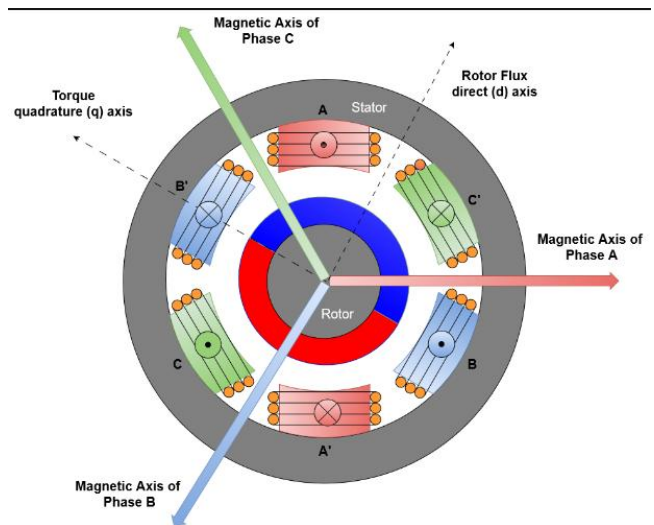


Figure 2.21 Stationary reference frame (ABC-Axis) and travelling reference frame(dq-axis) (Radonic, 2024)

and Park Transformations. Since the d-q-axes in the travelling reference frame are decoupled from each other, they simplify the representation of motor dynamics and are widely used to model PMLSMs.

A thesis by Cheema. M and an article by Miller C.E present the model of PMLSM in a two-axis travelling reference frame.¹⁰ In this model, they have neglected the losses due to eddy currents and thermal effects caused by stator resistances and permanent magnet flux. Initially, the electro-mechanical thrust force of the motor is quantified in terms of the power as shown in Eqn 2.21

$$F = \frac{\text{Electromechanical Power } (P_{em})}{\text{Mechanical speed } (v_m)} \quad (2.21)$$

$$P_{em} = V_{dq} i_{dq} \quad (2.22)$$

The voltage (V_{dq}) of the stator can be expressed in the d-q reference frame as shown in Eqn 2.23

$$V_d = R_s i_d + \frac{d\lambda_d}{dt} - \frac{P\pi v_m}{\tau} \lambda_q \quad ; \quad V_q = R_s i_q + \frac{d\lambda_q}{dt} + \frac{P\pi v_m}{\tau} \lambda_d \quad (2.23)$$

Where, λ_{dq} represents the the magnetic flux of from the stator coils, R_s represents the coil resistance, P represents the pole number of the permanent magnets, v_m represents the mechanical speed and τ represents the pole pitch. In Eqn 2.23, the magnetic flux of the stator coils (λ_{dq}) can be further written as shown in Eqn 2.24.

$$\lambda_d = L_s i_d + \lambda_f \quad ; \quad \lambda_q = L_s i_q \quad (2.24)$$

Where, L_s is the self-inductance of the stator coils and λ_f is the magnetic flux of the rotor's permanent magnets. Since the d-axis in the d-q reference frame is aligned with the rotor's magnetic flux, there is no magnetic flux present along the q-axis. Substituting Eqn 2.23 and Eqn 2.24 in Eqn 2.22, we get the expression for the instantaneous power as shown in Eqn 2.25.

$$P = \frac{3}{2} (R_s i_d^2 + R_s i_q^2) + \frac{3}{2} \frac{d}{dt} \left(\frac{1}{2} L_s i_d^2 + \frac{1}{2} L_s i_q^2 \right) + \frac{3}{2} \frac{\pi}{\tau} P v_m (\lambda_d i_d + \lambda_q i_q) \quad (2.25)$$

In the above equation, the $\frac{3}{2}(R_s i_d^2 + R_s i_q^2)$ corresponds to the resistive losses and $\frac{3}{2} \frac{d}{dt} (\frac{1}{2} L_s i_d^2 + \frac{1}{2} L_s i_q^2)$ corresponds to the rate of change of the stored energy. The active power represented by $\frac{3}{2} \frac{\pi}{\tau} P v_m (\lambda_d i_d + \lambda_q i_q)$ contributes to the generation of thrust force in the PMLSMs. Substituting the expression for the active power in Eqn 2.21, we obtain the thrust force of the motor as a function of the current and magnetic flux in the d-q reference frame as shown in Eqn 2.26.

$$F = \frac{3\pi P}{2\tau} (\lambda_d i_d + \lambda_q i_q) \quad (2.26)$$

Further simplifying Eqn 2.26 by substituting the magnetic flux expression from Eqn 2.24, we get the expression for the thrust force only as a function of current.

$$F = \frac{3}{2} \frac{\pi}{\tau} P \lambda_f i_q \quad (2.27)$$

In Eqn 2.27, the rotor permanent magnet flux (λ_f), pole pitch (τ) and pole number (P) are constants for a given PMLSM. Hence, the thrust force is linearly dependent on the current flowing through the stator windings. The constant term $\frac{3}{2} \frac{\pi}{\tau} P \lambda_f$ can be grouped in a single variable called as motor constant or K_t . Therefore, we can express the thrust force of the motor as shown in Eqn 2.28.

$$\text{Thrust Force } (F) = K_t * \text{Current } (i) \quad (2.28)$$

This theoretical derivation was studied by Cheema. It will be a helpful result that will be used in developing a state-space model for the exoskeleton gantry.

Chapter 3: Exoskeleton Gantry Modelling

3.1 Theoretical Model of Gantry

The exoskeleton gantry is modelled using equations of motion, and a state space model of the exoskeleton gantry is formulated. The state space model is used to generate the theoretical transfer functions and theoretical Bode plots of the system. The response of each axis is studied to lay out the predictions for the experimental data.

A free-body diagram of the exoskeleton gantry is shown in Figure 3.11. Initially, for modelling purposes, it was assumed that the tilt angle α caused due to differences in thrust from Y1 and Y2 stages is negligible. Furthermore, for the modelling of the vertical stages, it was assumed that the distances of the mass (M) from each of the vertical stages are equal, i.e. $l1 = l2$. Moreover, each stage of the gantry is assumed to have an independent current input. The vertical stages Y1 and Y2 are also assumed to be coupled for modelling.

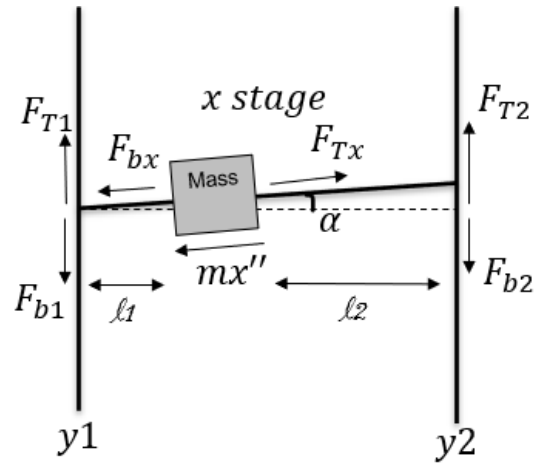


Figure 3.11 Exoskeleton Gantry Free-Body Diagram

Taking reference from the gantry model developed by Xie. H⁸, the center of mass of the load was used to formulate the equations of motion for each of the gantry stages.

$$\text{Stage X: } M\ddot{x} = F_{Tx} - b\dot{x} \quad (3.11)$$

$$\text{Stage Y: } M\ddot{y}_C = F_{Ty1} + F_{Ty2} - (b_1 + b_2)\dot{y}_C \quad (3.12)$$

The center of mass of the load is as shown in Eqn 3.13, and the equations of motion of the gantry are shown in Eqn 3.11 and Eqn 3.12.

$$y_c = \frac{l_1}{L}y_1 + \frac{l_2}{L}y_2 \quad (3.13)$$

Substituting Eqn 3.13 in Eqn 3.12, we get the equation of motion of the Stage Y.

$$\text{Stage Y: } \frac{M l_2 \ddot{y}_1}{L} + \frac{M l_1 \ddot{y}_2}{L} = F_{Ty_1} + F_{Ty_1} - b\dot{y}_1 - b\dot{y}_2 \quad (3.14)$$

A state-space model and transfer function were derived using Eqn (3.14) and Eqn (3.11). In these equations, the thrust force from the motor is modelled in terms of the force constant (K_t) and the input current. The state space model of the exoskeleton gantry is shown below, followed by the transfer function for each stage.

State Space Model

$$\dot{z} = Az + Bu$$

$$T = Cz$$

$$A \equiv \begin{bmatrix} 0 & 1 & 0 & 0 & 0 & 0 \\ 0 & \frac{-b}{M} & 0 & 0 & 0 & 0 \\ 0 & 0 & 0 & 1 & 0 & 0 \\ 0 & 0 & 0 & \frac{-bL}{2Ml} & 0 & \frac{-bL}{2Ml} \\ 0 & 0 & 0 & 0 & 0 & 1 \\ 0 & 0 & 0 & \frac{-bL}{2Ml} & 0 & \frac{-bL}{2Ml} \end{bmatrix} \quad B \equiv \begin{bmatrix} 0 & 0 & 0 \\ \frac{K_t}{M} & 0 & 0 \\ 0 & 0 & 0 \\ 0 & \frac{K_t L}{2Ml} & \frac{K_t L}{2Ml} \\ 0 & 0 & 0 \\ 0 & \frac{K_t L}{2Ml} & \frac{K_t L}{2Ml} \end{bmatrix}$$

$$C \equiv \begin{bmatrix} 0 & 1 & 0 & 0 & 0 & 0 \\ 0 & 0 & 0 & 1 & 0 & 0 \\ 0 & 0 & 0 & 0 & 0 & 1 \end{bmatrix} \quad u \equiv \begin{bmatrix} i_1 \\ i_2 \\ i_3 \end{bmatrix} \quad \dot{z} \equiv \begin{bmatrix} \dot{x} \\ \dot{v}_x \\ \dot{y}_1 \\ \dot{v}_{y_1} \\ \dot{y}_2 \\ \dot{v}_{y_2} \end{bmatrix}$$

Plant Transfer Functions

$$\text{Stage X: } P_x(s) \equiv \frac{v_x(s)}{I(s)} = \frac{K_t}{b + Ms} \quad (3.15)$$

$$\text{Stage Y: } P_y(s) \equiv \frac{v_y(s)}{I(s)} = \frac{K_t L}{2Mls + 2bL} \quad (3.16)$$

$K_t \equiv$ Motor Constant; $b \equiv$ Damping Coefficient; $L \equiv$ Motor Length; $M \equiv$ Mass; $l \equiv$ distance travelled by the load on the Stage X. The load is assumed to be centered on the Stage X for modelling purposes. The theoretical derivation of the state-space model and transfer function is shown in Appendix A

A block diagram of the exoskeleton gantry is shown in Figure 3.12. In this figure, the plant $P(s)$ is represented by the open loop transfer functions of X or Y stages, and the current controller is a PI controller with gains K_P and K_I . The closed-loop and open-loop transfer functions with the PI controller are derived using the block diagram as given below.

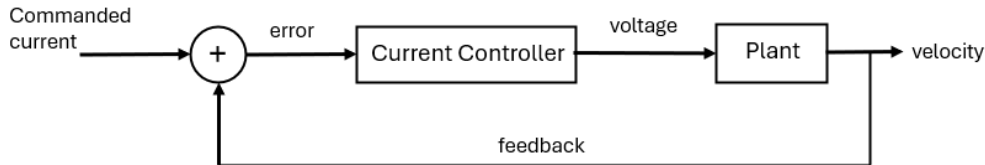


Figure 3.12 Closed-loop current controlled exoskeleton gantry block diagram.

Open Loop System with PI controller transfer functions

$$\text{Stage X: } G_x(s) \equiv \frac{v_x(s)}{I(s)} = \frac{K_t}{b + Ms} \left(K_P + \frac{K_I}{s} \right) \quad (3.17)$$

$$\text{Stage Y: } G_y(s) \equiv \frac{v_y(s)}{I(s)} = \frac{K_t L}{2Mls + 2bL} \left(K_P + \frac{K_I}{s} \right) \quad (3.18)$$

Closed-loop System with PI controller Transfer Functions

$$\text{Stage X: } G_x(s) \equiv \frac{v_x(s)}{I(s)} = \frac{(K_P s + K_I) K_t}{Ms^2 + s(b + K_P K_t) + K_I K_t} \quad (3.19)$$

$$\text{Stage Y: } G_y(s) \equiv \frac{v_y(s)}{I(s)} = \frac{K_t L (K_p s + K_I)}{2Mls^2 + s(2bL + K_t K_p L) + K_t L K_I} \quad (3.20)$$

The closed-loop transfer function was used to generate a theoretical Bode plot of the exoskeleton system. Expected values of the system constants were used to study the magnitude response of the theoretical closed-loop transfer function. The PI-USA permanent magnetic linear synchronous motor has ball bearings, which are predicted to have a damping coefficient within the range of 330 Ns/m – 550 Ns/m. The motor constant for the PI-USA direct drive motor is 20 N/A. and the motor length and payload are 0.8 m and 35 kg, respectively. Using these values as system constants, the Bode plots for stages X and Y are plotted as shown in Figure 3.13 and Figure 3.14, respectively.

Stage X

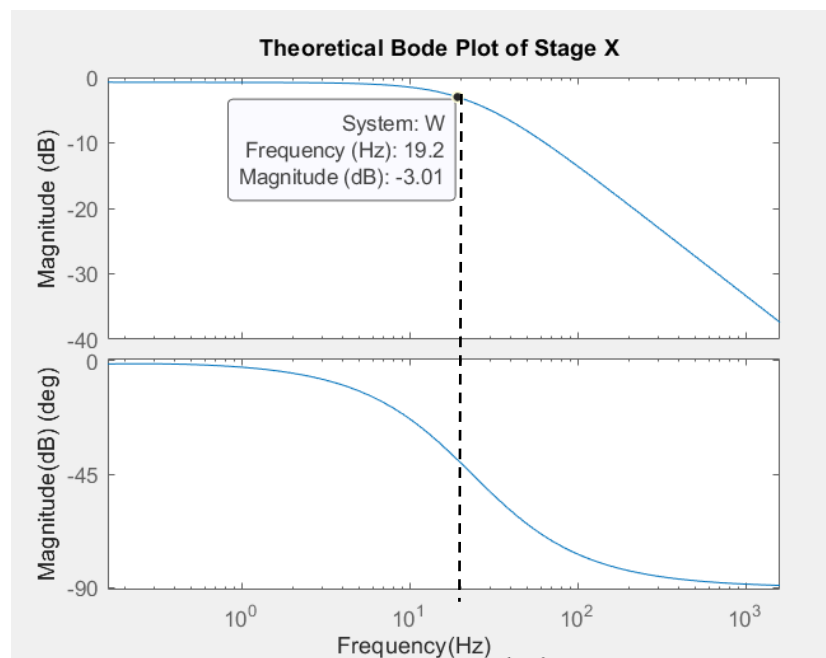


Figure 3.13a Theoretical bode plot of closed loop system for stage X. The bandwidth of the system is marked using the dotted line.

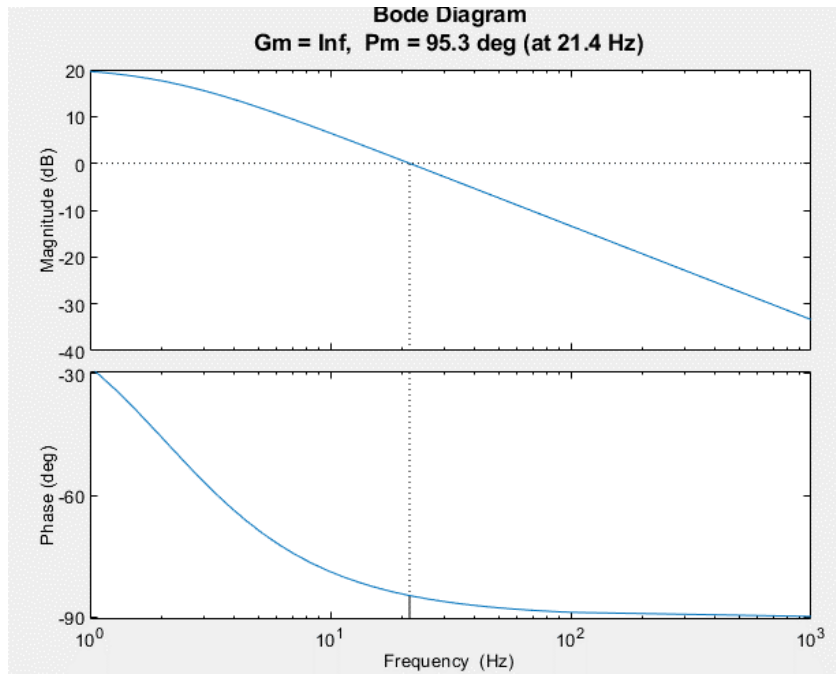


Figure 3.13b Theoretical open loop bode plot with gain and phase margin of stage X.

Stage Y

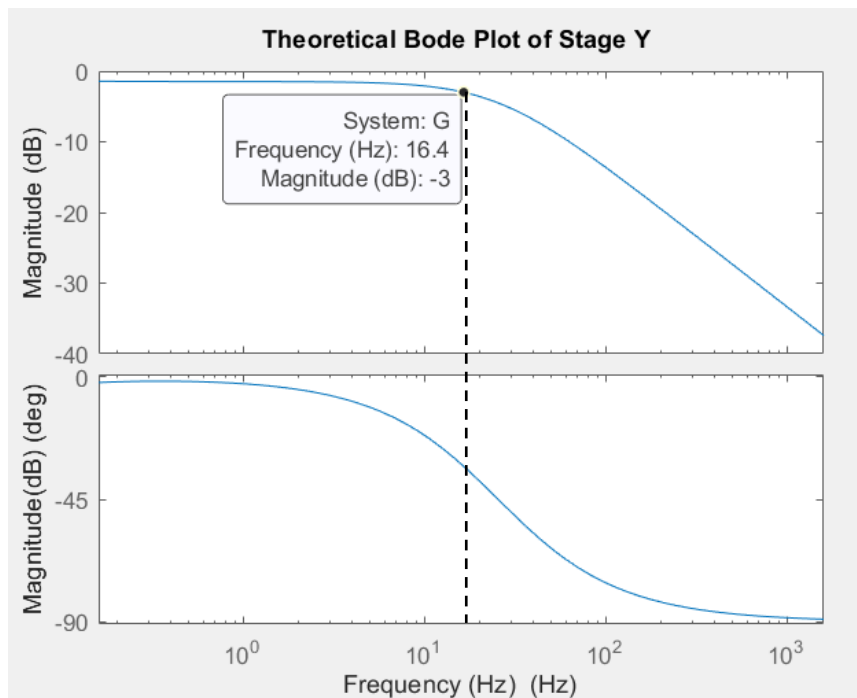


Figure 3.14a Theoretical magnitude plot of closed loop system for stage Y. The bandwidth of the system is marked using the dotted line.

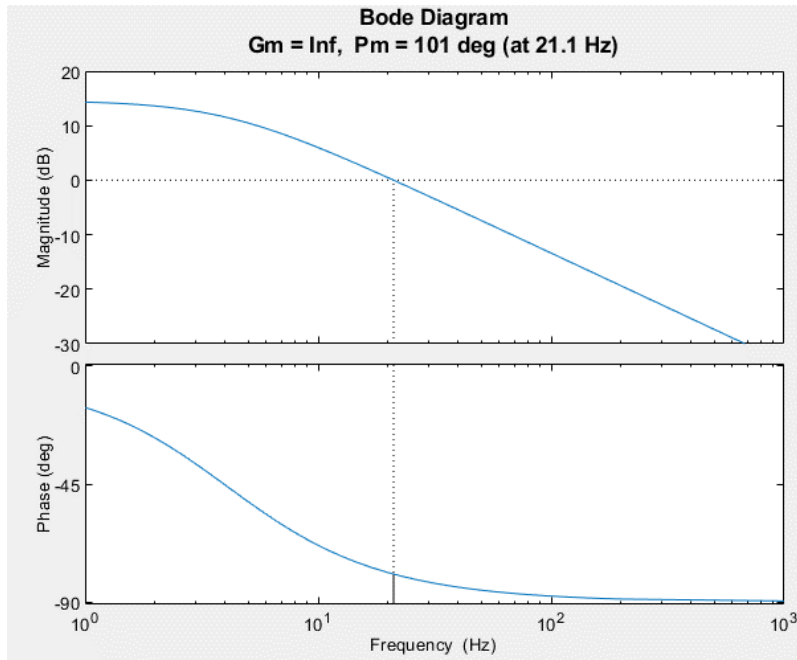


Figure 3.14b Theoretical open loop bode plot with gain and phase margin of stage Y.

As shown in Figure 3.13a and Figure 3.14a, the expected bandwidth of the closed-loop Stage X is approximately 19.2 Hz, whereas the expected bandwidth of closed-loop Stage Y is 16.4 Hz. The magnitude of the output is expected to reduce by -20 dB/decade if the input frequency is higher than the bandwidth of the system. The open-loop bandwidth is 3.8 Hz for Stage Y and 1.9 Hz for Stage X. The bandwidth of the open-loop system is low due to a pole at the origin of the integral controller. From inspection of the open loop gain and phase margin of each stage in Figure 3.13b and Figure 3.14b, we can conclude that both the stages can be expected to be stable with a phase margin of 95.3° and 101.0° for X and Y stages, respectively. Since the phase margin is greater than the desired value of 45° and the gain margin is higher than the desired value of 2 dB, the closed-loop system is expected to be stable. The phase margin is expected to increase with the decrease in payload for the system. Furthermore, the transfer function derived above suggests that the closed-loop system with the controller for Stage X and Y is a type 0 system, whereas the open-

loop system with the controller is a type 1 system. The system characteristics can be summarized as shown in Table 3.1.

Table 3.1 System characteristics of Current Loop of Stages X and Y.

<u>Characteristics</u>	<u>Stage Y</u>	<u>Stage X</u>
Closed Loop Bandwidth with PI controller (Hz)	16.4	19.2
Open Loop DC gain(dB)	14.7	20.8
Open Loop Bandwidth with PI controller (Hz)	3.8	1.9

3.2 Admittance Control

Admittance control is commonly used in human-robot interaction environments when the robot needs to respond to a stimulus. In admittance control, the interaction force between the user and robot is measured, and the motion controller is commanded accordingly using a set of pre-determined virtual dynamics.¹¹ The external interaction force from the user is measured using a force sensor and can be modelled using the inertial, damping, and stiffness of the gantry.

$$F_{ext} = m_v \ddot{x}_e + b_v \dot{x}_e + k_v x_e \quad (3.21)$$

$$x_e = x - x_d \quad (3.22)$$

In Eqn (3.21) and Eqn (3.22), x_e is the positional error, x is the real position and x_d is the desired/reference position of the robot. The constant m_v , b_v and k_v refer to the virtual mass, virtual damping and virtual stiffness for the virtual dynamics of the robot. The virtual dynamics in admittance control determine the reference position or velocity for the robot based on the external force experienced by it. Using the equations Eqn(3.21) and Eqn(3.22), we can derive the transfer function for the virtual dynamics for admittance control.

Virtual Dynamic Transfer Function

$$Y_v = \frac{\text{Velocity}}{\text{External Force}} = \frac{s}{m_v s^2 + b_v s + k_v} \quad (3.23)$$

A block diagram of admittance controller is shown in figure 3.21.

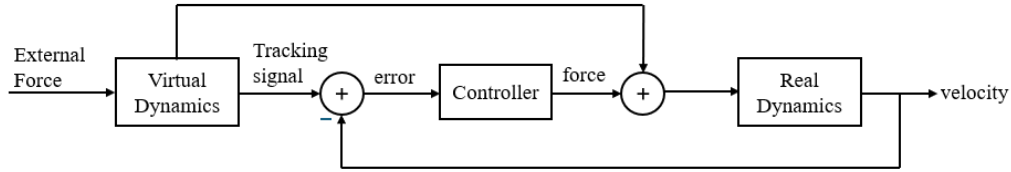


Figure 3.21 Generic Block Diagram of admittance control implementation

Admittance control is implemented on the exoskeleton gantry system, and the bandwidth of the admittance-controlled system is studied experimentally. For the exoskeleton system, it is assumed that the stiffness (k_v) of the gantry is negligible. Hence, the transfer function for virtual dynamics for the exoskeleton gantry becomes as follows:

Virtual Dynamics Transfer Function for gantry

$$Y_v = \frac{\text{Velocity}}{\text{External Force}} = \frac{1}{m_v s^2 + b_v} \quad (3.24)$$

The implementation of admittance control in the exoskeleton gantry is shown in Figure 3.22. The nested feedback loops represent the internal structure of the Copley controllers used in the study.

The closed loop admittance-controlled system as shown in Figure 3.22 is experimentally tested to

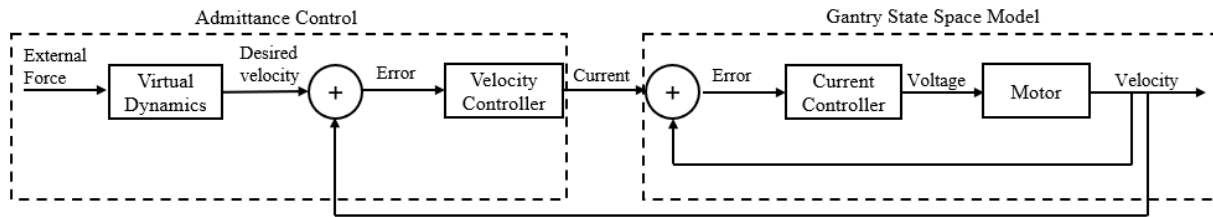


Figure 3.22 Block Diagram of exoskeleton gantry with admittance control implementation

determine the bandwidth of the system. For experimentation purpose, a desired velocity is specified to the system as input, and the actual velocity is the output.

Chapter 4: Experimental Verification

4.1 *Experimental Set-Up and Data Processing*

The bandwidth of the open-loop system and the stability of the closed-loop gantry model are experimentally verified, and the gain and phase margin are compared to the theoretical model. The gantry was previously set up with the cross-axis Stage X and parallel Stage Y. Each stage is independently actuated using LABVIEW. The Stage X is under a payload of 27 kg from the rotational stage and optic system, and each stage weighs approximately 16 kg. Figure 4.11 shows the exoskeleton gantry. A sinusoidal current signal input with an amplitude of 0.5 A is used for the

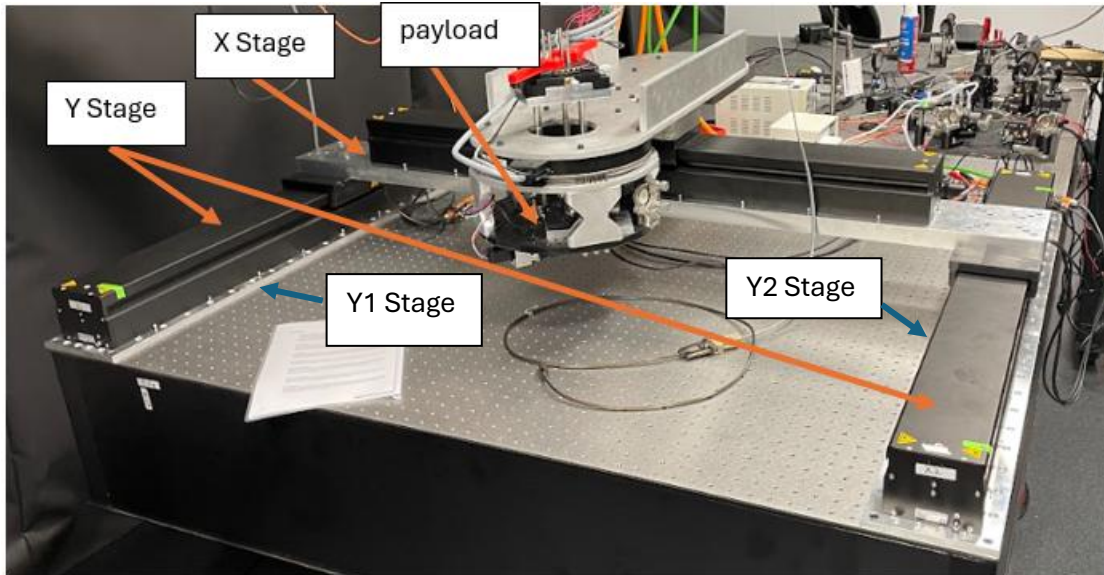


Figure 4.11 Setup of the exoskeleton gantry. The payload consists of the optic system setup on the rotation stage.

actuation of Stage X of the gantry. A current input signal with an amplitude of 1.75A is used for actuating the Stage Y of the gantry. Since Stage Y of the gantry must withstand a higher load compared to Stage X, a higher actuation current signal is needed for Stage Y. The frequency of the input current signal is swept from 1 Hz to 75 Hz. The sampling rate is 0.002 ms, and the total trace time for each batch of single-frequency data is 5 seconds. The velocity and position data corresponding to each frequency are stored for post-processing. Only the open loop system current

control is verified experimentally due to the inability of LABVIEW and the Copley control system to output the velocity with a current input in a closed-loop system setting. The open-loop data was used to make predictions about the closed-loop system.

The data processing is conducted using MATLAB signal processing toolbox. The MATLAB code for Stage X is shown in Appendix B-II, and the code for Stage Y is shown in Appendix B-I. The experimental data are processed using two methods. For the first method, the raw data is processed to derive the experimental gain. To calculate the gain at each frequency, the rms value of the output signal is calculated at the respective frequency, and the amplitude is computed from it. The gain is computed by dividing the output velocity/position amplitude by the input current signal amplitude. The gain in decibels is plotted against the frequency in hertz on a semilogarithmic scale to obtain the experimental Bode plots of the exoskeleton system.

For the second method, the previously derived gain and its respective frequency is concatenated using **'idfrd'** function in MATLAB. This function is used to create frequency response data (FRD) models from frequency response measurements or transfer functions. It stands for "Identified Frequency Response Data." The frequency response data model serves as an argument for **'tfest'** function in MATLAB. Inferences from the theoretical model were used to specify the number of poles and zeroes for the system. The theoretical model suggests that the open-loop system with a PI controller for X and Y stages is a second-order system with one zero. This inference is used in experimental modelling. The **'tfest'** function is used for estimating continuous-time or discrete-time transfer function models from time-domain input-output data. Since the gain starts decreasing with increasing frequency, the data at higher frequencies can have higher noise interference. To prevent the MATLAB model from learning the noise, a weighting

system was introduced. Higher weight was given to data at lower frequency, and lower weight was given to data at higher frequency.

Following the open-loop system verification, the admittance-controlled closed-loop system was experimentally tested, and the bandwidth was noted. A Copley controller was used to send an input signal of a desired velocity value, and the output is the real velocity of the gantry. The amplitude of the desired velocity is set to 12.5 mm/s, and the frequency of the input signal was swept from 5 Hz to 250 Hz.

4.2 Results

The experimental verification results of open open-loop gantry system for X and Y stages are shown in Figure 4.21 and Figure 4.22. Both the Stage Y motors were coupled for actuation to prevent noise due to resistance and friction from their subordinate motor.

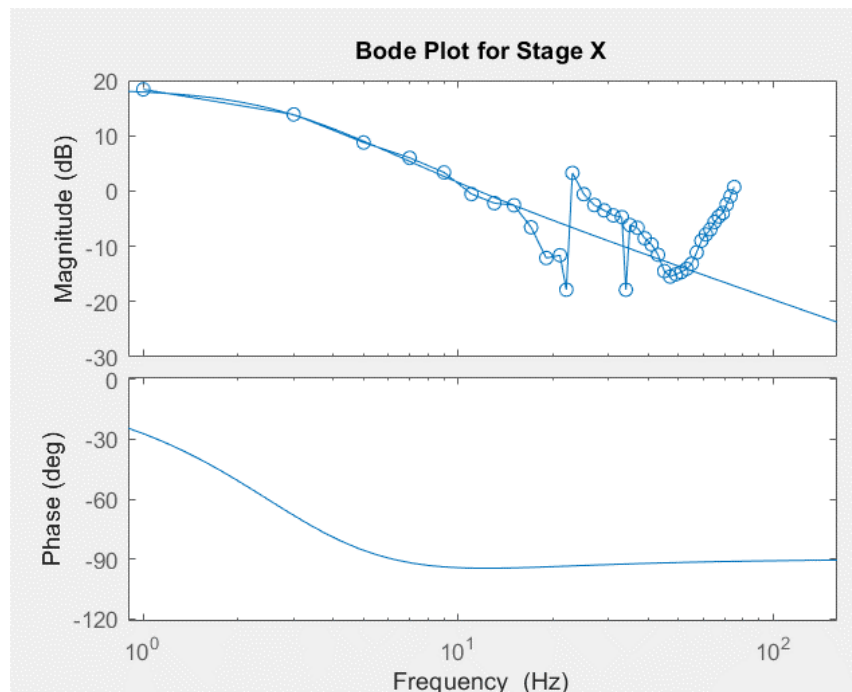


Figure 4.21 Experimental open-loop bode plot for Stage X. The experimental data is shown with the individual data points, while the MATLAB estimated model using 'fpest' is shown with the continuous line.

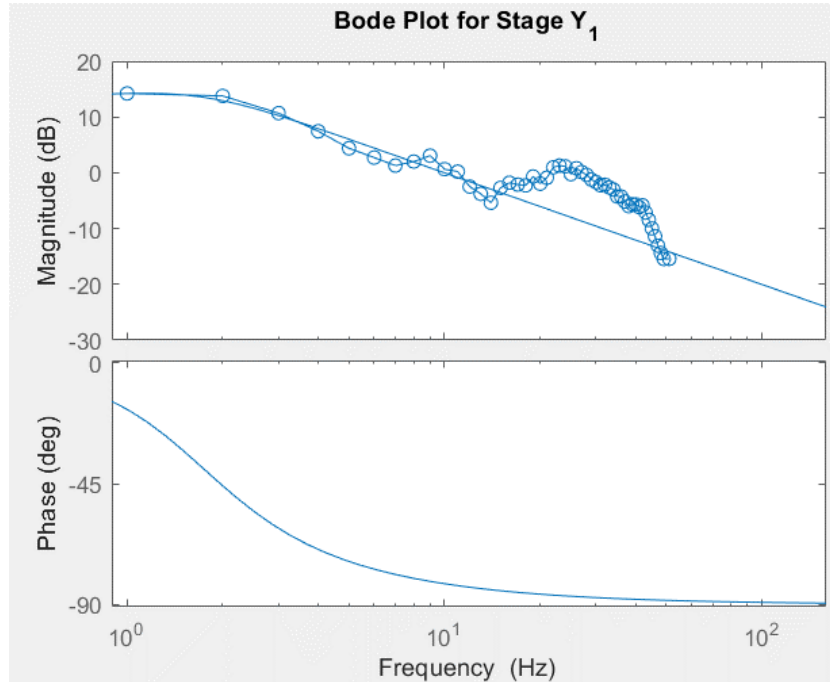


Figure 4.22a Experimental open-loop bode plot for Y1 stage. The experimental data is shown with the individual data points, while the MATLAB estimated model using 'ffest' is shown with the continuous line.

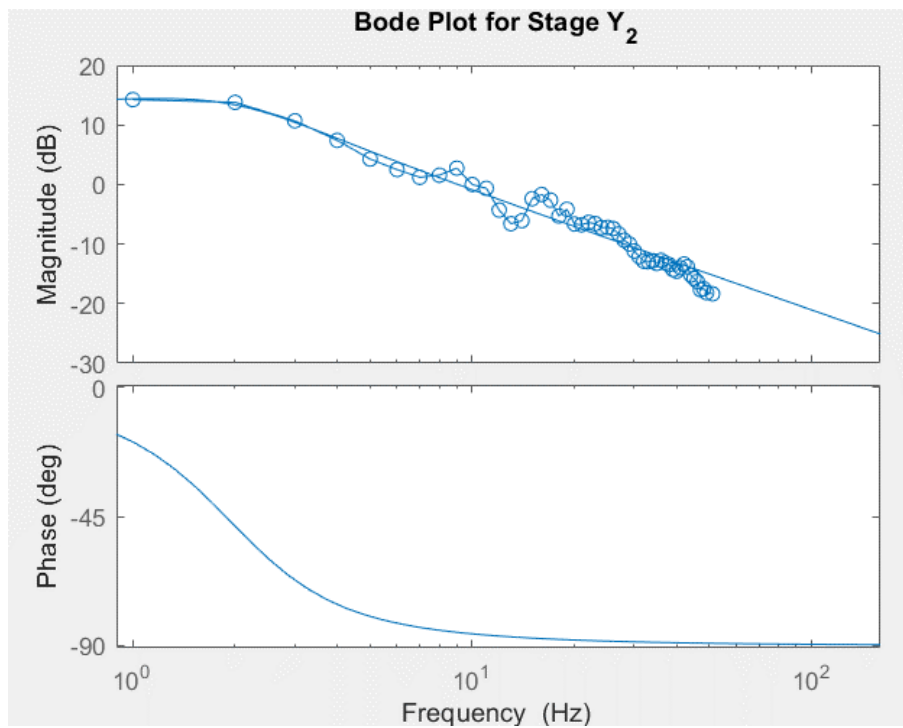


Figure 4.22b Experimental open loop bode plot for Y2 stage. The experimental data is shown with the individual data points, while the MATLAB estimated model using 'ffest' is shown with the continuous line.

The open experimental results can be summarized as shown in Table 4.21.

Table 4.1 Summary of open-loop experiment results for X and Y stages.

Characteristic	Stage X	Stage Y1	Stage Y2
Open Loop Bandwidth (Hz)	2.3	2.73	2.8
DC gain(dB)	18	14.4	14.3

The gain and phase margin were also estimated using the transfer function model generated by MATLAB using the experimental input and output data. The gain and phase margin plots are shown in Figures 4.23 and 4.24.

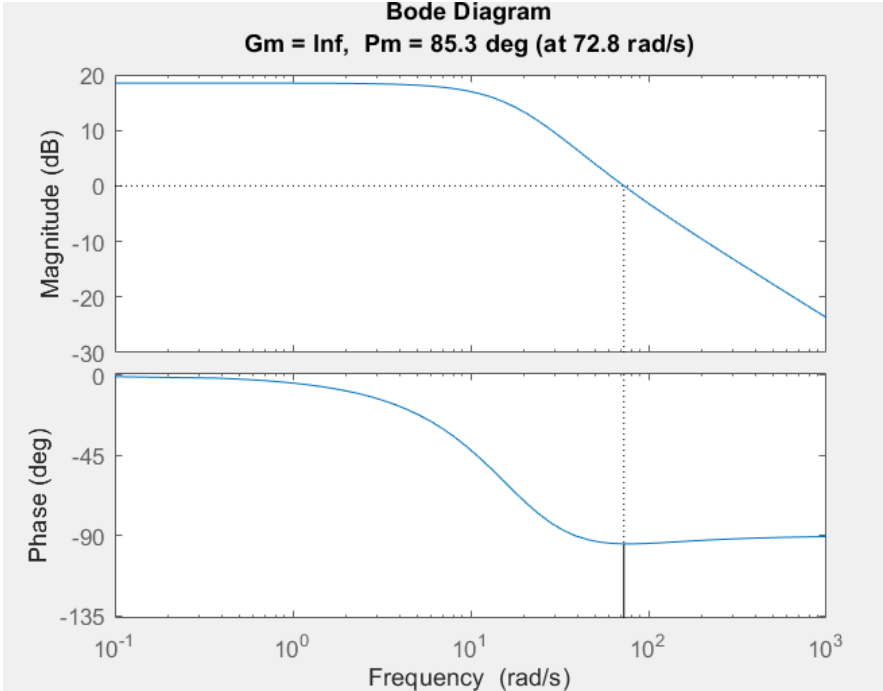


Figure 4.23 Experimental Open Loop Gain and Phase Margin of Stage X

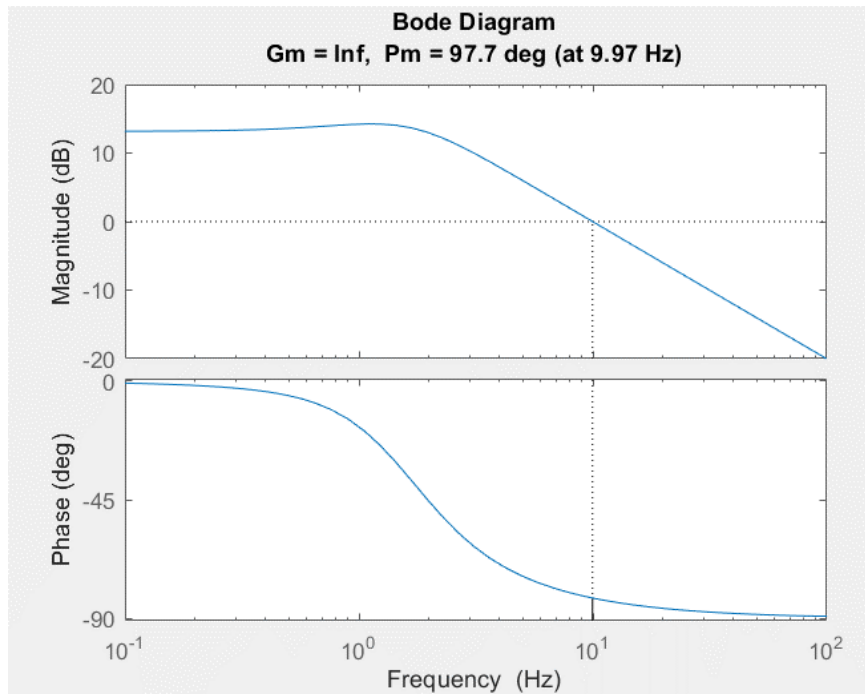


Figure 4.24a Experimental Open Loop Gain and Phase Margin of Stage Y1

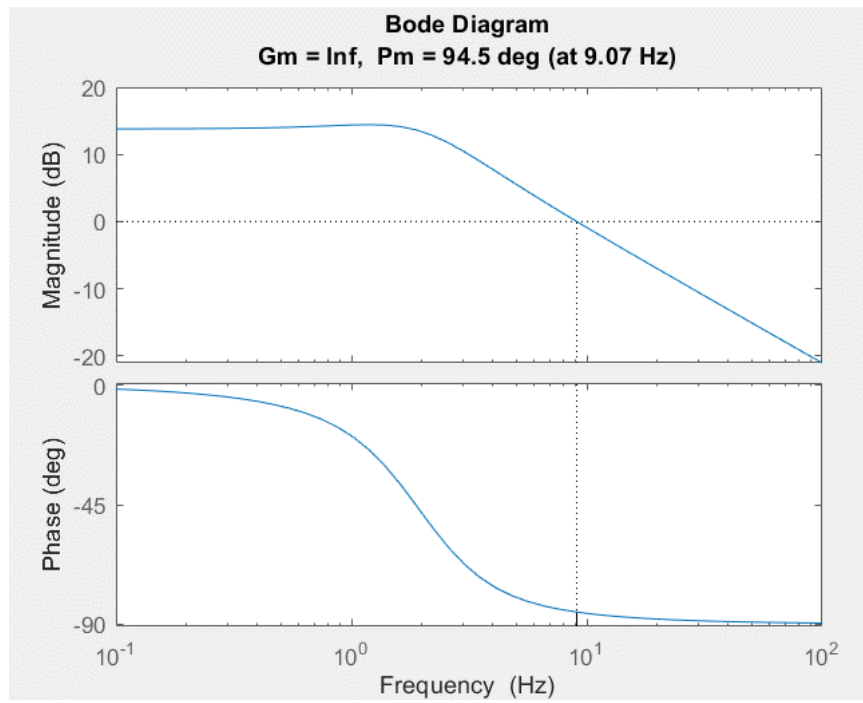


Figure 4.24b Experimental Open Loop Gain and Phase Margin of Stage Y2

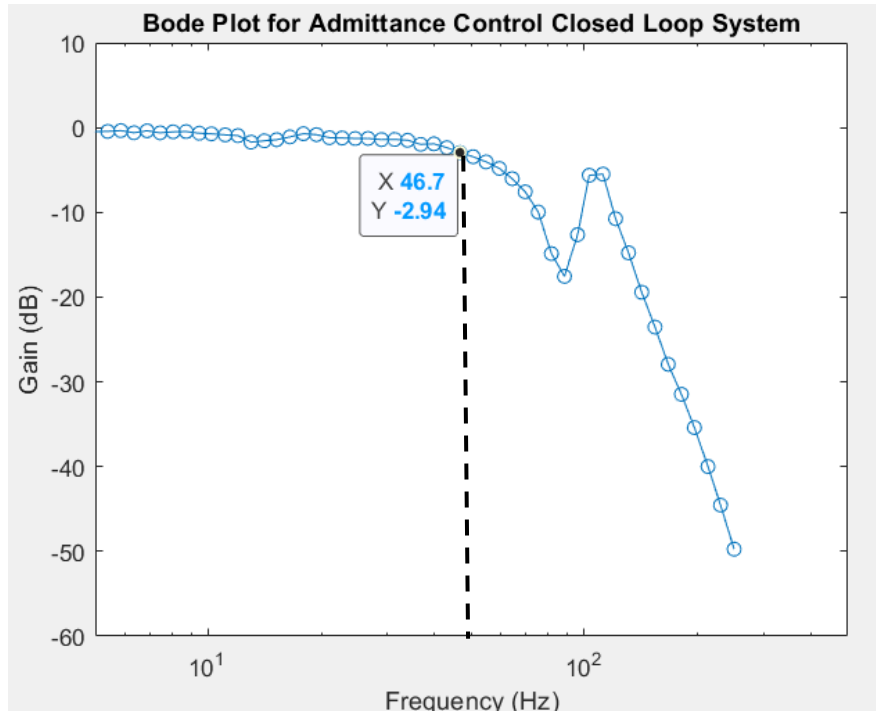


Figure 4.25 Closed Loop Admittance Controlled Stage X Bode Plot

As seen from Figure 4.23 and Figure 4.24, the gain margin is sufficiently above the desired value of 2dB, while the phase margin is sufficiently above the desired value of 45 degrees and hence, the actual closed-loop system can be expected to be stable.

Furthermore, the admittance-controlled closed-loop system is studied experimentally and the results are summarized as shown in Figure 4.25. Since the Copley controller requires decoupling of the stages to provide input-output signals, only Stage X is studied to obtain an experimental estimate of experimental bandwidth as Stage Y needs to be coupled together to provide reliable data. The bandwidth of the admittance-controlled closed-loop system is found to be 46 Hz.

4.3 *Discussion*

Taking reference from the theoretical gantry model result from Table 3.1, the bandwidth of the open-loop system for X and Y stages is expected to be 1.9 Hz and 3.8 Hz, respectively. The bandwidth of the open system, as determined experimentally (refer to Table 4.1), is found to be 2.3 Hz for Stage X and 2.76 Hz for Stage Y. The experimental bandwidth of Stage Y is slightly lower than the theoretically determined bandwidth, while the experimental bandwidth of Stage X is slightly higher than the theoretical bandwidth. Moreover, the experimental and theoretical results both suggest that the open-loop bandwidth of Stage Y is higher than the bandwidth of Stage X. This can be related to the payload experienced by each stage during actuation. For the sake of theoretical analysis, each stage is assumed to experience the same payload, and the average payload experienced by the stages is used for the analysis. However, in reality, the payload experienced by Stage Y is higher compared to Stage X. This is attributed to Stage Y bearing the payload of the optic system, alongside supporting the weight of Stage X resting upon it. Whereas the payload experienced by Stage X is only the optics system. It can be shown using the derived theoretical model that the bandwidth of the open-loop gantry system decreases by increasing the payload experienced by it. Using the open-loop gantry model derived previously in Chapter 3, along with a PI controller, the bandwidth of X and Y stages is computed for different payloads ranging from 5 kg to 40 kg. The increase in bandwidth with a decrease in payload using this analysis is shown in Figure 4.31.

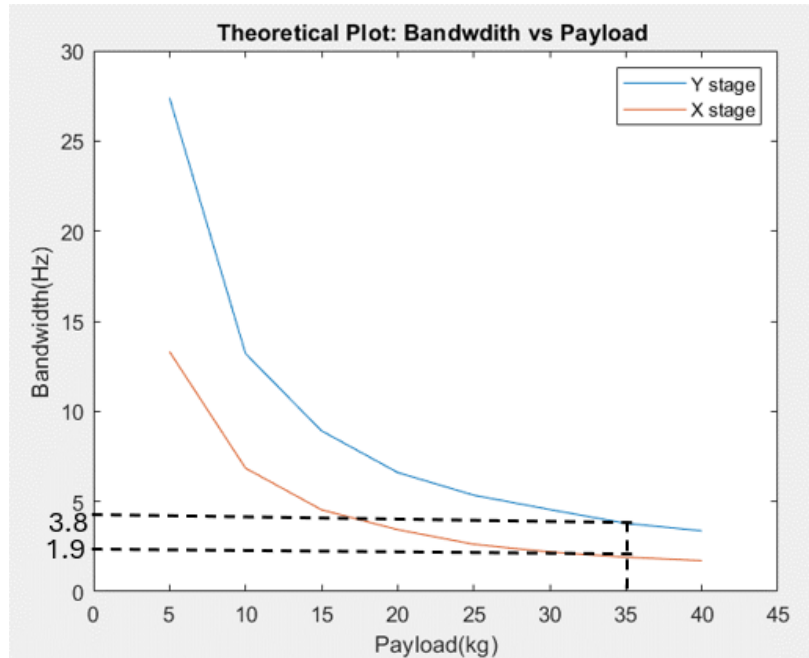


Figure 4.31 Theoretical Plot of Bandwidths of Open Loop Gantry for X and Y stages over a range of payloads.

From Figure 4.31, we can see that the bandwidth exponentially decreases with an increase in payload experienced by the gantry. This explains the lower bandwidth of the experimental Stage Y as compared to the theoretical data and the higher bandwidth of the experimental Stage X compared to the theoretical results. However, even though Stage Y had a higher payload, it still had a higher bandwidth compared to Stage X with a lower payload. This is because the thrust force exerted by Stage Y is twice as large as Stage X. Since Stage Y is comprised of two coupled motors in a parallel setting, the higher payload experienced by it is counteracted by a higher thrust force compared to Stage X. Hence, Stage Y has a higher bandwidth compared to Stage X despite a greater payload.

The DC gain of the open-loop system, as found experimentally, is approximately 14.35 dB for Stage Y and 18 dB for Stage X. While the DC gain of the X and Y stages, as found using theoretical analysis, is 20.8 dB and 14.7 dB, respectively. The experimental DC gain for Stage X is slightly lower than the expected DC gain found using theoretical analysis. The

discrepancies between the experimental and theoretical DC gain could also be attributed to inaccuracies in component values, variations in manufacturing tolerances, and effects of parasitic elements not fully accounted for in the theoretical analysis.

Furthermore, it can be noted that the predicted closed-loop bandwidth is higher than the theoretical and experimental open-loop bandwidth. This can be explained using a key feature of closed-loop and open-loop systems. Gain and bandwidth of a system are inversely proportional to each other. Since the gain of a closed-loop system decreases due to the addition of negative feedback, the bandwidth of a closed-loop system is expected to increase compared to an open-loop system.

Lastly, the experimental and theoretical gain and phase margin analysis both confirm the stability of the closed-loop gantry system. In order for a closed-loop system to be stable, the open-loop gain margin needs to be greater than 20dB, and the phase margin needs to be greater than 45 degrees. According to the results, the phase and gain margin of the experimental and theoretical system is well above the desired values.

Chapter 6: Conclusion and Future Work

In this thesis, a theoretical dynamic model of an exoskeleton gantry robot is developed to study important system characteristics. The bandwidth of the open-loop and closed-loop gantry with a PI controller is studied along with the gain and phase margins to ensure closed-loop system stability. The bandwidth of the open-loop X and Y stages is predicted to be 1.9 Hz and 3.8 Hz, respectively, using the theoretical model, while the bandwidth of the closed-loop model is predicted to be 19.2 Hz and 16.4 Hz for the X and Y stages, respectively. The open-loop gantry model is experimentally verified using LABVIEW, and an experimental model of the exoskeleton gantry is obtained using the System Identification toolbox in MATLAB. The experimental bandwidth of the open-loop system is found to be 2.3 Hz for Stage X, 2.73 Hz for Y₁ Stage, and 2.8 Hz for Y₂ Stage. Moreover, the gain and phase margin of the open-loop model found theoretically and experimentally is higher than the desired gain margin of 20dB and phase margin of 45 degrees. This confirms the stability of the closed-loop system. Furthermore, admittance control is proposed for the exoskeleton gantry, and the bandwidth of the closed-loop admittance control model is determined using preliminary experimentation. The bandwidth of admittance-controlled closed-loop exoskeleton gantry is found to be 46 Hz for Stage X.

Since only preliminary experimentation is conducted for the admittance-controlled system, as an extension of this work, the bandwidth of the coupled Stage Y with admittance control needs to be studied as well. Additionally, exploration of methods to reduce the system's payload could be pursued to verify the resulting increase in both open-loop and closed-loop bandwidths. Moreover, the rotational stage of the gantry and the interaction effects between the different stages can be accounted for in the theoretical modelling of the gantry to obtain a more thorough dynamic model of the exoskeleton gantry.

APPENDIX

APPENDIX A – Theoretical Plant Transfer Function Derivation

System Equations

$$\text{Stage X: } M\ddot{x} = F_{Tx} - b\dot{x}$$

$$\text{Stage Y: } \frac{M l_2 \dot{y}_1}{L} + \frac{M l_1 \dot{y}_2}{L} = F_{Ty1} + F_{Ty2} - b\dot{y}_1 - b\dot{y}_2$$

$$\text{Thrust Force: } F_T = K_t i$$

State Space Equations

$$v_x = \dot{x}$$

$$M\dot{v}_x = K_t i_3 - b v_x$$

$$v_{y1} = \dot{y}_1 ; v_{y2} = \dot{y}_2$$

$$\frac{M l_2 \dot{v}_{y1}}{L} + \frac{M l_1 \dot{v}_{y2}}{L} = K_t i_1 + K_t i_2 - b v_{y1} - b v_{y2}$$

State Space Model

$$\begin{bmatrix} \dot{x} \\ \dot{v}_x \\ \dot{y}_1 \\ \dot{v}_{y1} \\ \dot{y}_2 \\ \dot{v}_{y2} \end{bmatrix} = \begin{bmatrix} 0 & 1 & 0 & 0 & 0 & 0 \\ 0 & \frac{-b}{M} & 0 & 0 & 0 & 0 \\ 0 & 0 & 0 & 1 & 0 & 0 \\ 0 & 0 & 0 & \frac{-bL}{2Ml} & 0 & \frac{-bL}{2Ml} \\ 0 & 0 & 0 & 0 & 0 & 1 \\ 0 & 0 & 0 & \frac{-bL}{2Ml} & 0 & \frac{-bL}{2Ml} \end{bmatrix} \begin{bmatrix} x \\ v_x \\ y_1 \\ v_{y1} \\ y_2 \\ v_{y2} \end{bmatrix} + \begin{bmatrix} 0 & 0 & 0 \\ \frac{K_t}{M} & 0 & 0 \\ 0 & 0 & 0 \\ 0 & \frac{K_t L}{2Ml} & \frac{K_t L}{2Ml} \\ 0 & 0 & 0 \\ 0 & \frac{K_t L}{2Ml} & \frac{K_t L}{2Ml} \end{bmatrix} \begin{bmatrix} i_1 \\ i_2 \\ i_3 \end{bmatrix}$$

$$\begin{bmatrix} v_x \\ v_{y1} \\ v_{y2} \end{bmatrix} = \begin{bmatrix} 0 & 1 & 0 & 0 & 0 & 0 \\ 0 & 0 & 0 & 1 & 0 & 0 \\ 0 & 0 & 0 & 0 & 0 & 1 \end{bmatrix} \begin{bmatrix} x \\ v_x \\ y_1 \\ v_{y1} \\ y_2 \\ v_{y2} \end{bmatrix}$$

State Space to Transfer Function

$$TF = C^{-1}(s * I - A) * B$$

Solved using Mathematica:

```
In[13]:= (*b=damping coeff.m=
         payload L=motor-length y=y K=force-constant*)
aMatrix = {{0, 1, 0, 0, 0, 0}, {0, -b/m, 0, 0, 0, 0},
           {0, 0, 0, 1, 0, 0}, {0, 0, 0, -L*b/(2*m*y), 0,
           -L*b/(2*m*y)}, {0, 0, 0, 0, 0, 1},
           {0, 0, 0, -L*b/(2*m*y), 0, -L*b/(2*m*y)}};
bMatrix = {{0, 0, 0}, {(K/m), 0, 0}, {0, 0, 0},
           {0, K*L/(2*m*y), K*L/(2*m*y)}, {0, 0, 0},
           {0, K*L/(2*m*y), K*L/(2*m*y)}};
cMatrix = {{0, 1, 0, 0, 0, 0}, {0, 0, 0, 1, 0, 0}, {0, 0, 0, 0, 0, 1}};
Simplify[
  MatrixForm[cMatrix.Inverse[s * IdentityMatrix[6] - aMatrix].
    bMatrix]]

Out[16]//MatrixForm=

$$\begin{pmatrix} \frac{K}{b+ms} & 0 & 0 \\ 0 & \frac{KL}{2bL+2msy} & \frac{KL}{2bL+2msy} \\ 0 & \frac{KL}{2bL+2msy} & \frac{KL}{2bL+2msy} \end{pmatrix}$$

```

Figure A.1 Snippet of Mathematica code and output. The non-diagonal entries correspond to interaction effects between the axis, whereas the diagonal entries correspond to the transfer function for the input/output of the same stage.

Plotting Code

```
clear; clc;
close all;
y = 0.4; %distance travelled by motor - input
payload = 35; % kg
damping_coeff = 440
motor_length = 0.8; %m
force_constant = 20; % N/A
Ki = 94/2 ;
Kp = 236 ;

s = tf('s');
G_open = ((force_constant * motor_length)*(Kp*s + Ki))/(2* (damping_coeff *
motor_length * s + payload * s^2 * y));
W_open= ((Ki/s + Kp)*force_constant)/(damping_coeff + payload*s);
G = ((force_constant * motor_length)*(Kp*s + Ki))/(2*payload * s^2 * y + s* (2 *
damping_coeff * motor_length + force_constant * motor_length * Kp) + force_constant *
motor_length * Ki);
```

```

W = ((Kp*s+ Ki) * force_constant)/(s^2 *payload + s * damping_coeff + (Kp*s + Ki) *
force_constant)
p = bodeoptions('cstprefs');
p.FreqUnits = 'Hz';
options = bodeoptions;
options.FreqUnits = 'Hz';
options.XLim = {[10^0 10^3]};
options.Title.FontWeight = 'bold';
options.Title.FontSize = 10;
margin(W_open,options)

figure;
margin(G_open, options)
%title('Gain and Phase Margin Plot of Stage Y')

figure;
bode(G,{10^0, 10^4}, p)
title('Theoretical Bode Plot of Stage Y ')
xlabel('Frequency (Hz)')
ylabel('Magnitude(dB)')
figure;
bode(W,p, {10^0, 10^4})
title('Theoretical Bode Plot of Stage X ')
xlabel('Frequency(Hz)')
ylabel('Magnitude(dB)')

```

APPENDIX B – Experimental Results Processing Code

I) STAGE Y Code

```

clear; clc;
close all;

% Read data from an Excel file into a table

data_table = readtable('C:\Eesha\0_Research\Documents from
PinHao\20240306_copley_scope_double_actuation_stage_12.xlsx', 'Range', 'A1',
'ReadVariableNames', false);

% Load data
frequency = data_table.Var2;
current = data_table.Var3;
vel_x1 = data_table.Var6;
vel_x2 = data_table.Var7;
freq_Hz = unique(frequency);

% Create a cell array to store current arrays for each frequency
currentCell = cell(1, length(freq_Hz));
vel_x1Cell = cell(1, length(freq_Hz));
vel_x2Cell = cell(1, length(freq_Hz));

```

```

for i = 1:length(freq_Hz)
    % Find indices corresponding to the current frequency
    indices = find(freq_Hz(i) == frequency);

    % Store the current values in the cell array
    currentCell{i} = current(indices);
    vel_x1Cell{i} = vel_x1(indices);
    vel_x2Cell{i} = vel_x2(indices);
end

for i = 1 : length(freq_Hz)

    Camp = sqrt(2) * sqrt(mean(currentCell{i}.^2));
    current_amp(i) = Camp;
    vel_x1amp = sqrt(2) * sqrt(mean(vel_x1Cell{i}.^2));
    vel_x_1_amp(i) = vel_x1amp;
    vel_x2amp = sqrt(2) * sqrt(mean((vel_x2Cell{i}).^2));
    vel_x_2_amp(i) = 100 *vel_x2amp;

end

for i = 1: length(freq_Hz)
    gain_x1(i) = vel_x_1_amp(i)/current_amp(i);
    gain_x1_dB = 20 * log10(gain_x1 );
    gain_x2(i) = vel_x_2_amp(i)/current_amp(i);
    gain_x2_dB = 20 * log10(gain_x2);
    freq_rad(i) = freq_Hz(i) * 2 * pi;
end

% Transpose data
freq_rad = freq_rad(1:50).';           % Transpose freq_rad
vel_x_1_amp = vel_x_1_amp. ';         % Transpose vel_x_1_amp
current_amp = current_amp. ';        % Transpose current_amp
vel_x_2_amp = vel_x_2_amp. ';
gain_x1 = gain_x1(1:50);
gain_x2 = gain_x2(1:50);
gain_x1_dB = gain_x1_dB(1:50);
gain_x2_dB = gain_x2_dB(1:50);
% Create iddata objects
frequency = frequency(1:50) * 2 * pi
sys_data_x1 = idfrd(gain_x1,freq_rad,0,'FrequencyUnit','rad/s');
sys_data_x2 = idfrd(gain_x2,freq_rad,0,'FrequencyUnit','rad/s');

% Initialize weight vector with ones
Weight = ones(size(frequency));

%Iterate over frequency values
for i = 1:50
    % Check if frequency is less than 20 Hz
    if freq_Hz(i) < 20
        Weight(i) = 20; % Assign weight of 10
    else
        Weight(i) = Weight(i) / 2; % Divide weight by 10
    end
end

```

```

    end
end

opt = tfestOptions('WeightingFilter',Weight, 'EnforceStability',true);
sys_tf_x1 = tfest(sys_data_x1,2,1,opt)
sys_tf_x2 = tfest(sys_data_x2,2,1,opt)
freq_range_decades = logspace(0.75, 3, 1000);
p = bodeoptions('cstprefs');
p.FreqUnits = 'Hz';

% Plot for vel_x_1_amp
figure;
semilogx(freq_Hz(1:50), gain_x1_dB, '-o');
title('Semilogarithmic Plot for posx1amp');
xlabel('Frequency (Hz)');
ylabel('Gain(dB)');
hold on;
bode(sys_tf_x1,p,{10^0.75 10^3});
title('Bode Plot for Stage Y_1');
hold off;

% Plot for vel_x_2_amp
figure;
semilogx(freq_Hz(1:50), gain_x2_dB, '-o');
title('Semilogarithmic Plot for posx2amp');
xlabel('Frequency (Hz)');
ylabel('Gain(dB)');
hold on;
bode(sys_tf_x2, p,{10^0.75 10^3});
title('Bode Plot for Stage Y_2');
hold off;

figure;
margin(sys_tf_x1, p)

figure;
margin(sys_tf_x2, p)

```

II) STAGE X Code

```

clear; clc;
close all;

data_table = readtable('C:\Eesha\0_Research\Documents from
PinHao\Stage_3_Labview.xlsx', 'Range', 'A1', 'ReadVariableNames', false);

% Load data
frequency = data_table.Var2;
current = data_table.Var3;
vel_x = data_table.Var6;

```

```

freq_Hz = unique(frequency);

% Create a cell array to store current arrays for each frequency
currentCell = cell(1, length(freq_Hz));
vel_xCell = cell(1, length(freq_Hz));

for i = 1:length(freq_Hz)
    % Find indices corresponding to the current frequency
    indices = find(freq_Hz(i) == frequency);

    % Store the current values in the cell array
    currentCell{i} = current(indices);
    vel_xCell{i} = vel_x(indices);
end

for i = 1 : length(freq_Hz)

    Camp = sqrt(2) * sqrt(mean(currentCell{i}.^2));
    current_amp(i) = Camp;
    vel_xamp = sqrt(2) * sqrt(mean(vel_xCell{i}.^2));
    vel_x_amp(i) = vel_xamp;

end

for i = 1: length(freq_Hz)
    gain_x(i) = vel_x_amp(i) /current_amp(i);
    gain_x_dB = 20 * log10(gain_x );
    freq_rad(i) = freq_Hz(i) * 2 * pi;
end

% Transpose data
vel_x_amp = vel_x_amp.'; % Transpose vel_x_1_amp
current_amp = current_amp.'; % Transpose current_amp

% Create iddata objects
frequency = frequency * 2 * pi;
sys_data_x = idfrd(gain_x,freq_rad,0, 'FrequencyUnit', 'rad/s');

% Initialize weight vector with ones
Weight = ones(length(freq_rad), 2);

% Iterate over frequency values
for i = 1:length(freq_rad)
    % Check if frequency is less than 20 Hz
    if freq_Hz(i) < 20
        Weight(i, :) = [0, 20]; % Assign weight of 20 for frequencies less than
10 Hz
    else
        Weight(i, :) = [0.5, 1]; % Assign weight of 0.5 for frequencies greater
than or equal to 10 Hz
    end
end
end

```

```

opt = tfestOptions('WeightingFilter',Weight, 'EnforceStability',true);
sys_tf_X = tfest(sys_data_x,2,1,opt);
bandwidth(sys_tf_X)
freq_range_decades = logspace(0.75, 3, 1000);
figure;
margin(sys_tf_X)
p = bodeoptions('cstprefs');
p.FreqUnits = 'Hz';

% Plot for Stage X
figure;
semilogx(freq_Hz, gain_x_dB, '-o');
title('Semilogarithmic Plot for posx1amp');
xlabel('Frequency (Hz)');
ylabel('Gain(dB)');
hold on
bode(sys_tf_X, p, {10^0.75 10^3});

title('Bode Plot for Stage X');
hold off

figure;
margin(sys_tf_X,p)

```

References

- 1) Stosiek, C., Garaschuk, O., Holthoff, K., & Konnerth, A. (2003, May 30). *In vivo two-photon calcium imaging of neuronal networks*. Proceedings of the National Academy of Sciences of the United States of America. <https://doi.org/10.1073/pnas.1232232100>
- 2) Grienberger, C., Giovannucci, A., Zeiger, W., & Portera-Cailliau, C. (2022, September 1). *Two-photon calcium imaging of neuronal activity*. Nature Reviews Methods Primers. <https://doi.org/10.1038/s43586-022-00147-1>
- 3) Pinto, L., Koay, S. A., Engelhard, B., Yoon, A. M., Deverett, B., Thiberge, S. Y., Witten, I. B., Tank, D. W., & Brody, C. D. (2018, March 6). *An Accumulation-of-Evidence Task Using Visual Pulses for Mice Navigating in Virtual Reality*. Frontiers in Behavioral Neuroscience. <https://doi.org/10.3389/fnbeh.2018.00036>
- 4) Rynes, M. L., Surinach, D., Linn, S., Laroque, M., Rajendran, V., Dominguez, J., Hadjistamoulou, O., Navabi, Z. S., Ghanbari, L., Johnson, G., Nazari, M., Mohajerani, M. H., & Kodandaramaiah, S. B. (2021, April 1). *Miniaturized head-mounted microscope for whole-cortex mesoscale imaging in freely behaving mice*. Nature Methods. <https://doi.org/10.1038/s41592-021-01104-8>
- 5) Hope, J., Beckerle, T., Cheng, P., Viavattine, Z., Feldkamp, M. D., Fausner, S. M. L., Saxena, K., Ko, E., Hryb, I., Carter, R. E., Ebner, T. J., & Kodandaramaiah, S. B. (2023, June 6). *Brain-wide neural recordings in mice navigating physical spaces enabled by a cranial exoskeleton*. bioRxiv (Cold Spring Harbor Laboratory). <https://doi.org/10.1101/2023.06.04.543578>
- 6) Chen, R., Yan, L., Zhang, J., & Shang, Y. (2019, January 1). *Dynamic modeling and analysis of flexible H-type gantrStage Y*. Journal of Sound and Vibration. <https://doi.org/10.1016/j.jsv.2018.09.047>
- 7) Qin, C., Zhang, C., & Lu, H. (2017, December 1). *H-Shaped Multiple Linear Motor Drive Platform Control System Design Based on an Inverse System Method*. Energies. <https://doi.org/10.3390/en10121990>
- 8) Xie, H., & Wang, Q. (2022, August 19). *Modeling Dual-Drive GantrStage Ys with Heavy-Load and Optimal Synchronous Controls with Force-Feed-Forward Decoupling*. Entropy. <https://doi.org/10.3390/e24081153>
- 9) *Modelling a permanent magnet linear synchronous motor for control purposes*. (2002). IEEE Conference Publication | IEEE Xplore. <https://doi.org/10.1109/AFRCON.2002.1159992>
- 10) *A Linear Quadratic Regulator-Based Optimal Direct Thrust Force Control of Linear Permanent-Magnet Synchronous Motor*. (2016, May 1). IEEE Journals & Magazine | IEEE Xplore. <https://doi.org/10.1109/tie.2016.2519331>

11) Keemink, A. Q. L., Van Der Kooij, H., & Stienen, A. (2018, April 29). *Admittance control for physical human–robot interaction*. The International Journal of Robotics Research. <https://doi.org/10.1177/0278364918768950>

12) Radonic. (2024, January 3). *Mastering motor control: motor control 101*. Embedded. Retrieved April 25, 2024, from <https://www.embedded.com/mastering-motor-control-motor-control-101/>.